CWI

Centrum voor Wiskunde en Informatica
Centre for Mathematics and Computer Science

J.J. Rusch

The use of defect-correction for the solution
of the 2-D compressible Navier-Stokes equations
with large Reynolds number

The Use of Defect-Correction for the Solution of

the 2-D Compressible Navier-Stokes Equations

with Large Reynolds Number

Jurgen Jan Rusch

Centre for Mathematics and Computer Science
P.O. Box 4079, 1009 AB Amsterdam, The Netherlands

We solve the 2-dimensional compressible Navier-Stokes equations by means of a defect-correction process. The approximate problems solved in the iteration are described by the Euler equations with a source term. The discretization method applied is a finite volume method. The auxiliary problems are solved by a Multi-Grid technique.
First, as a test problem, Poiseuille-flow is simulated at a low Mach number. The numerical solutions are compared with the solutions of the incompressible Navier-Stokes equations.
Next, a channel model is used with a Mach number of approximately 0.85 at the inlet. Finally, the same model is considered, but now with a circular bump on its lower wall. No special grid refinements are made to resolve the boundary layers.
If more detailed solutions were desired, computer simulations should have been made with higher resolutions of the grid, especially near the wall. Nevertheless, the numerical solutions give a good qualitative impression of the global behaviour of the solution of the Navier-Stokes equations.

1. INTRODUCTION

The Navier-Stokes equations describe the motion of a compressible fluid, taking into account viscosity and heat conduction. In two dimensions the state of a compressible gas is represented by a vector quantity q in $\mathbb{R}^4$. As state variables one can select for example the quantities $\rho, \rho u, \rho v$ and ρe, denoting respectively the density, density of momentum in x- and y-direction, and total energy density. If q and the equation of state are known, all other state variables such as pressure p, enthalpy $h = e + p / \rho$, entropy $s = p\rho^{-\gamma}$, $z = ln(s)$, temperature, speed of sound, $c = (\gamma p / \rho)^{1/2}$, Mach number etc. can be derived.

Generally, the state of a gas varies in space and time. If there is no time-dependency, the flow is said to be steady, which is the type of flow we are interested in here.

Assuming the equation of state to be $p = \rho RT$ (perfect gas), the two-dimensional Navier-Stokes equations for compressible fluids in a region $\Omega^* \subset \mathbb{R}^2$ are

$$\frac{\partial}{\partial t}q + \frac{\partial}{\partial x} F(q) + \frac{\partial}{\partial y} G(q) = 0 , \tag{1.1a}$$

where

$$F(q) = f(q) - \frac{1}{\text{Re}} f^{(v)}(q) ,$$
$$G(q) = g(q) - \frac{1}{\text{Re}} g^{(v)}(q) . \tag{1.1b}$$

The fluxes f and g are defined by :

$$f = \begin{bmatrix} \rho u \\ \rho u^2 + p \\ \rho uv \\ \rho uh \end{bmatrix} , \quad g = \begin{bmatrix} \rho v \\ \rho uv \\ \rho v^2 + p \\ \rho vh \end{bmatrix} , \tag{1.2a}$$

and $f^{(v)}$ and $g^{(v)}$ by

$$f^{(v)} = \begin{bmatrix} 0 \\ \sigma_x \\ \tau_{xy} \\ \zeta(c^2)_x + u\sigma_x + v\tau_{xy} \end{bmatrix} , \quad g^{(v)} = \begin{bmatrix} 0 \\ \tau_{xy} \\ \sigma_y \\ \zeta(c^2)_y + u\tau_{xy} + v\sigma_y \end{bmatrix} . \tag{1.2b}$$

Here $\zeta = \kappa / (\gamma - 1)Pr$, where κ denotes the heat-conductivity of the gas, and where Re and Pr are the problem-dependent Reynolds and Prandtl number.

The quantities σ_x , σ_y and τ_{xy} are arguments of the stress tensor $\mathbb{T}$, which is defined by

$$\mathbb{T} = \begin{bmatrix} \sigma_x & \tau_{xy} \\ \tau_{xy} & \sigma_y \end{bmatrix} = \begin{bmatrix} \lambda (u_x + v_y) + 2\mu u_x & \mu(u_y + v_x) \\ \mu(u_y + v_x) & \lambda (u_x + v_y) + 2\mu v_y \end{bmatrix} . \tag{1.3}$$

The scalars λ and μ are two viscosity parameters and we will assume Stokes' hypothesis of zero bulk-viscosity, i.e.

$$3\lambda + 2\mu = 0 . \tag{1.4}$$

It should be emphasized that (1.1) and (1.2) are the non-dimensional form of the Navier-Stokes equations.

The vector quantities F and G are the Navier-Stokes fluxes in x- and y- direction, f and g the so-called Euler-fluxes in these directions, and $f^{(v)}$ and $g^{(v)}$ the viscous fluxes. The Navier-Stokes flux in the (n_x , n_y)-direction is then given by

$$n_x . F(q) + n_y . G(q) ,$$

and similarly we can describe the Euler and viscous flux in this direction.

Basically the Navier-Stokes equations are conservation laws. They describe: the conservation of mass, momentum (in x- and y- direction) and energy. The first equation in (1.1) is the law of conservation of mass in differential form. Usually it is referred to as the continuity equation. The second and third equations are the momentum equations and describe laws of conservation of momentum in x-direction (second equation) and y-direction (third equation). The fourth equation is the law of conservation of energy in differential form and is referred to as the energy equation.

The derivation of the Navier-Stokes equations can be found in text-books on fluid dynamics such as [1],[2] or [3]. This derivation is beyond the scope of this work and will not be given here.

The steady Navier-Stokes equations form an elliptic system of non-linear second order partial differential equations (see e.g. [4]).
If the viscous and heat conduction terms are neglected, (1.1) reduces to the Euler equations. Then we have

$$F(q) = f(q) , \quad G(q) = g(q) . \tag{1.5}$$

The time-dependent Euler equations form a hyperbolic system of non-linear first order partial differential equations. By hyperbolic we mean that, when they are written in the quasi-linear form

$$\frac{\partial q}{\partial t} + \frac{\partial f}{\partial q} . \frac{\partial q}{\partial x} + \frac{\partial g}{\partial q} . \frac{\partial q}{\partial y} = 0 , \tag{1.6}$$

the matrix

$$k\,A + l\,B = k\,\frac{\partial f}{\partial q} + l\,\frac{\partial g}{\partial q} \tag{1.7}$$

has real eigenvalues for all directions (k,l). These eigenvalues are $ku + lv \pm c$ and $ku + lv$ (which is a double eigenvalue). The sign of the eigenvalues determines the positive or negative direction in which the information about the corresponding eigenvectors is travelling along lines pointing in the direction (k,l).

One of the important consequences of the non-linearity of the Euler equations is that their solutions may become discontinuous. Since shocks, i.e. discontinuities, are difficult to formulate by means of differential equations, the integral form of (1.1) can be used to describe the flow with a shock. This form is obtained by integrating (1.1) over an arbitrary region $\Omega \subset \Omega^*$. We then get :

$$\frac{\partial}{\partial t} \iint_\Omega q \, dxdy + \int_{\partial\Omega} (\, n_x F + n_y G \,) \, ds = 0 \, , \qquad \text{for all } \Omega \subset \Omega^* \, . \tag{1.8}$$

By $\partial\Omega$ we mean the boundary of Ω, and by $(n_x \, , n_y)$ the outward normal vector on $\partial\Omega$. In a more compact form we write (1.8) as

$$q_t + N(q) = 0 \, . \tag{1.9}$$

Thus, we replace the partial differential operators by a single (non-linear) operator $N(q)$. This operator can be split into an Euler part and a viscous part, i.e.

$$N(q) = E(q) - \frac{1}{\text{Re}} \cdot V(q) \, . \tag{1.10}$$

To obtain a steady state solution of (1.3) we require $\partial q \,/\, \partial t$ to vanish. This leads to the non-linear equation

$$N(q) = 0 \, . \tag{1.11}$$

In some (relatively) simple cases, solutions of (1.11) have been obtained analytically. This is the case e.g. with the Couette-flow through a channel.(see e.g. [3]) In practice however, one is interested in more complex flow-models, such as the flow around an airfoil.

To solve the Navier-Stokes equations for models where the solution cannot be given in closed form, one has to find a numerical solution. Of course one wishes to use a discretization which represents the physical model as good as possible and with as little computational effort as possible.

2. Discretization of the Navier-Stokes equations

In order to discretize equation (1.11) on a domain Ω^* with an irregular grid there are essentially two different ways.

First, a mapping from the physical domain to a computational domain can be used, which maps the irregular grid in the physical domain onto a regular grid in the computational domain. Then the equations and boundary conditions are reformulated for the computational domain. The new equations will contain metric information about the mapping. Finally, a discretization of these transformed equations is used on the regular grid, thus solving the original problem.

The second approach is a technique in which the equations are discretized in the physical domain directly. This is the method that we used here. The discretization we used was the finite-volume method.

In figure 1 an irregular grid in the (x,y)-plane is shown. It has been obtained by mapping a rectangular regular grid in the (ξ,η)-plane.

$$\begin{cases} x = x\,(\xi\,,\,\eta\,) \\ y = y\,(\xi\,,\,\eta\,) \end{cases} , \quad (x,y) = M(\xi,\eta) \, . \tag{2.1}$$

The grid points (i,j) in the (ξ,η) and the (x,y)-plane are defined by

$$\begin{cases} \xi_{i,j} = (i - \tfrac{1}{2}) h_\xi \\ \eta_{i,j} = (j - \tfrac{1}{2}) h_\eta \end{cases} \quad \text{and} \quad \begin{cases} x_{i,j} = x(\xi_{i,j}, \eta_{i,j}) \\ y_{i,j} = y(\xi_{i,j}, \eta_{i,j}) \end{cases}, \qquad (2.2)$$

and the grid lines in the regular grid are defined by $\xi = i\, h_\xi$ and $\eta = j\, h_\eta$. The parameters h_ξ and h_η, grid spacings in ξ and η direction respectively, are fixed numbers for a given level of refinement. The mapping M divides the domain Ω^* in the physical space into a number of disjunct quadrilateral cells Ω_{ij}. To represent the solution, a set of 4-tuples q_h is used. Every element q_{ij} of q_h represents the (mean) value of the solution q on Ω_{ij}, i.e. the averaged state of the fluid in this volume.

To solve the Navier-Stokes equations in integral form, we require (1.8) to hold on every Ω_{ij} and thus we obtain the equation

$$\text{meas}(\Omega_{ij}) \cdot \frac{d}{dt} q_{ij} + \int_{\partial\Omega_{ij}} (n_x F + n_y G)\, ds = 0, \text{ for all } \Omega_{ij} \subset \Omega, \qquad (2.3)$$

where $n_x F + n_y G$ denotes the normal (Navier-Stokes-) flux outward Ω_{ij}. This implies that, for a steady solution of the Navier-Stokes equations, we require that

$$\sum_{k=N,E,S,W} \int_{\Gamma_{ijk}} (n_x F + n_y G)\, ds = 0, \text{ for all i,j}. \qquad (2.4)$$

Actually, for every k the integral in (2.4) is a rate of transport of q over the boundary Γ_{ijk}.

In a discretization, the flux $n_x F + n_y G$ in (2.4) is approximated by a **numerical** Navier-Stokes **flux**, which is evaluated for each k. Since F and G are both composed of an Euler and a viscous term, (2.4) can be rewritten as

$$\sum_{k=N,E,S,W} \int_{\Gamma_{ijk}} (n_x f + n_y g) - \frac{1}{\text{Re}} (n_x f^{(v)} + n_y g^{(v)})\ ds = 0, \text{ for all i,j}. \qquad (2.5)$$

The term with the fluxes f and g is approximated by a numerical Euler flux, and the other term by a numerical viscous flux.

The Euler-flux in an arbitrary direction was discretized by Osher's scheme [6] in a modified version as used by Hemker & Spekreijse [9]. In computations for Euler-flows this scheme has shown a good shock capturing. We will not discuss this scheme here.

Our goal is to discretize the viscous part of (2.5). As we see in (1.2b), for the computation of the Navier-Stokes flux it is necessary to evaluate $u_x, u_y, v_x, v_y, (c^2)_x$ and $(c^2)_y$. We have to evaluate these derivatives on each Γ_{ijk}.

3. DISCRETIZATION OF THE VISCOUS FLUX TERMS

We repeat the viscous terms in (1.2b) :

$$f^{(v)} = \begin{bmatrix} 0 \\ \sigma_x \\ \tau_{xy} \\ \zeta(c^2)_x + u\sigma_x + v\tau_{xy} \end{bmatrix}, \quad g^{(v)} = \begin{bmatrix} 0 \\ \tau_{xy} \\ \sigma_y \\ \zeta(c^2)_y + u\tau_{xy} + v\sigma_y \end{bmatrix}, \qquad (3.1a)$$

with

$$\sigma_x = \lambda(u_x + v_y) + 2\mu\, u_x,$$

$$\sigma_y = \lambda(u_x + v_y) + 2\mu\, v_y, \qquad (3.1b)$$

$$\tau_{xy} = \mu \left(u_y + v_x \right).$$

We shall show how to discretize the viscous fluxes (3.1a) for use in (2.5).

There are two quantities that we shall treat first. These are u and v that appear in (3.1a). Since we want to discretize (3.1a) on side AB (figures 2 and 3) the obvious choice for u and v is :

$$\begin{cases} u_{AB} = u_{i+\frac{1}{2},j} = \frac{1}{2} \left(u_{i,j} + u_{i+1,j} \right) \\ v_{AB} = v_{i+\frac{1}{2},j} = \frac{1}{2} \left(v_{i,j} + v_{i+1,j} \right). \end{cases} \tag{3.2}$$

If side AB is part of the boundary, u and v are known by the boundary condition which prescribes certain values at the wall AB.

To evaluate any partial derivative we use the method as outlined by Peyret & Taylor [10]. As an illustration we calculate u_x and u_y. Partial derivatives of v and c^2 are calculated similarly.

Suppose we want to evaluate u_x and u_y on side AB (fig. 3). First we approximate these values by the mean values of u_x and u_y on cell Ω' bounded by A',B',C' and D'. So we have :

$$\left[\frac{\partial u}{\partial x} \right]_{AB} = \frac{1}{\text{meas}(\Omega')} \int_{\Omega'} \frac{\partial u}{\partial x} \, d\sigma = \frac{1}{\text{meas}(\Omega')} \int_{\Gamma'} u \, n_x \, ds \,,$$

$$\left[\frac{\partial u}{\partial y} \right]_{AB} = \frac{1}{\text{meas}(\Omega')} \int_{\Omega'} \frac{\partial u}{\partial y} \, d\sigma = \frac{1}{\text{meas}(\Omega')} \int_{\Gamma'} u \, n_y \, ds \,. \tag{3.3}$$

The linear integrals are approximated by :

$$\int_{\Gamma'} u \, n_x = u_S \, \Delta y_{A'B'} + u_B \, \Delta y_{B'C'} + u_P \, \Delta y_{C'D'} + u_A \, \Delta y_{D'A'} \,, \tag{3.4a}$$

$$\int_{\Gamma'} u \, n_y = -u_S \, \Delta x_{A'B'} - u_B \, \Delta x_{B'C'} - u_P \, \Delta x_{C'D'} - u_A \, \Delta x_{D'A'} \,. \tag{3.4b}$$

The value of u at point P is known. However, the value of u at S,A and B is not always known.

First we treat u_S. If side AB is not a boundary-side then it is clear that the value $u_{i+1,j}$ can be used for u_S. But if AB is a boundary-side, u_S is calculated by extrapolating u_P and $u_{i+\frac{1}{2},j}$. The latter value is obtained by using a boundary condition at the boundary AB.

The values u_A and u_B remain to be evaluated. We will concentrate on u_B since u_A is computed similarly. For point B we will look at three different cases, which depend on the position of B within the grid, with respect to the boundaries.

a. Neither AB nor BC are boundary-sides (fig. 3). In this case a good approximation for u_B is given by

$$u_B = \frac{1}{4} \left(u_{i,j} + u_{i,j+1} + u_{i+1,j} + u_{i+1,j+1} \right). \tag{3.5a}$$

Assuming that u_B^* is the exact value at B, one can easily derive the following relation between u_B and u_B^* by Taylor expansion

$$u_B = u_B^* + \frac{1}{2} h_\xi^2 \left(x_{\xi\xi} + r^2 x_{\eta\eta} \right) \cdot \frac{\partial u}{\partial x} + \frac{1}{2} h_\xi^2 \left(y_{\xi\xi} + r^2 y_{\eta\eta} \right) \cdot \frac{\partial u}{\partial y} + \cdots. \tag{3.5b}$$

The quantity r denotes the ratio h_η / h_ξ. Second order derivatives of u with respect to x and y have been omitted in (3.5b). Suppose that $r=1$. Then we see that the error $u_B - u_B^*$ is first order with respect to u_x and u_y if x and y are non-harmonic functions of ξ and η. But if x and y are harmonic we see that this error is second order in the derivatives of u with respect to x and y. In both cases the error is second order with respect to the grid spacings h_ξ and h_η, as one can check by working out the terms with second order derivatives of u to x and y.

b. AB is a boundary-side and BC is not (figure 4). In this case a good approximation for u_B is given

by :

$$u_B = \frac{1}{2} (u_{i+\frac{1}{2},j} + u_{i+\frac{1}{2},j+1}) . \tag{3.6a}$$

The values $u_{i+\frac{1}{2},j}$ and $u_{i+\frac{1}{2},j+1}$ are obtained by using the boundary conditions on the respective sides. As in the previous case we can use Taylor expansion to obtain an expression for the error in u_B, resulting in

$$u_B = u_B^* + \frac{1}{8} h_\eta^2 (x_{\xi\xi} \frac{\partial u}{\partial x} + y_{\xi\xi} \frac{\partial u}{\partial y}) + \cdots , \tag{3.6b}$$

again omitting terms with second order derivatives of u with respect to x and y. We see that in general this method is first order in u_x and u_y. The error is second order in terms of the grid spacing, as we saw in case a.

c. Both AB and BC are boundary-sides (figure 5). In this case we approximate u_B by the arithmetic mean of two values that result from extrapolation. The first extrapolated pair is $u_{i,j+\frac{1}{2}}$, $u_{i-1,j+\frac{1}{2}}$ and the second pair is $u_{i+\frac{1}{2},j}$, $u_{i+\frac{1}{2},j-1}$. This results in

$$u_B = \frac{1}{4} (- u_{i-1,j+\frac{1}{2}} + 3 u_{i,j+\frac{1}{2}} + 3 u_{i+\frac{1}{2},j} - u_{i+\frac{1}{2},j-1}) . \tag{3.7a}$$

Again Taylor-expansion results in a relation between the exact value of u in B and the approximate value, namely :

$$u_B = u_B^* - \frac{3}{16} h_\xi^2 (x_{\xi\xi} + r^2 x_{\eta\eta}) \frac{\partial u}{\partial x} - \frac{3}{16} h_\xi^2 (y_{\xi\xi} + r^2 y_{\eta\eta}) \frac{\partial u}{\partial y} + \cdots \tag{3.7b}$$

As in case a, the error is second order in the derivatives of u if, for $r = 1$ the functions x and y are harmonic. For the non-harmonic case the error is first order in u_x and u_y. Again, the error is second order in the grid spacings h_ξ and h_η.

Thus, we have treated all cases for point B. From (3.5b) and (3.7b) we see that it would be a nice property if the following relations for x and y would hold :

$$\begin{cases} x_{\xi\xi} + r^2 x_{\eta\eta} = 0 , \\ y_{\xi\xi} + r^2 y_{\eta\eta} = 0 . \end{cases} \tag{3.8a}$$

If $r = 1$ equation (3.8) states that x and y are harmonic functions of ξ and η, i.e.

$$\begin{cases} x_{\xi\xi} + x_{\eta\eta} = 0 , \\ y_{\xi\xi} + y_{\eta\eta} = 0 . \end{cases} \tag{3.8b}$$

This is why many grids are generated by so called 'elliptic grid generators': most errors in approximations become second order.

4. TREATMENT OF THE BOUNDARY CONDITIONS

Since the compressible Navier-Stokes equations form an elliptic system of coupled partial differential equations, the solution is uniquely determined if a Dirichlet or Neumann boundary condition is used for every component of the solution on every part of the boundary. Whether this solution describes a physically realistic flow depends on the boundary conditions that are used.

In our model problems in section 6, three basically different types of boundaries are treated, viz.

    a. subsonic inflow boundary,
    b. subsonic outflow boundary and
    c. solid wall with no-slip condition.

At inflow we use Dirichlet conditions for the four components in the solution. The velocity vector as

well as two thermodynamic quantities are prescribed.

At outflow we always prescribe the pressure. The other solution components are determined by using the characteristics of the Euler equations. This boundary condition was used e.g. by Hemker & Spekreijse [9] for solving the compressible 2-dimensional Euler equations, yielding good results.

The use of Euler boundary-conditions for Navier-Stokes equations means that, implicitly, the Navier-Stokes boundary conditions are selected such that the viscous flux at that boundary vanishes. Indeed, in our models we assume the viscous flux at the outlet to be small enough to be neglected.

Now we are left with the treatment of a solid wall where a no-slip condition is imposed. Suppose that we want to know the state at point B in figure 6. The state in point I, a point within the flow, is (u_I, v_I, c_I, z_I). The components u_I and v_I denote the velocity with respect to the coordinate system as drawn in figure 6. The angle between this vector and the x-axis is α.

The state in B is determined by assuming a Couette flow in cell Ω_I, i.e. assuming that the compressibility enters only through temperature effects.

The state in B is described by four quantities, of which three are already known: the normal and tangential velocity components in B are 0 (no-slip condition!) and the pressure in B, which is taken to be equal to that at I. Only one more state-variable is needed.

This missing variable is obtained by using the relation (cf. Liepmann & Roshko [3], p. 309)

$$c_p \, T_B = c_p \, T_I + Pr \left(\frac{u_I^2}{2} + \frac{q_w}{\tau_w} \, u_I \right),$$ (4.1)

where T_B and T_I are the temperature at the boundary and the inner point respectively. By c_p we denote the specific heat at constant pressure (Couette-flow!). The quantities q_w and τ_w denote the heat flux through the wall and the shear stress along the wall respectively.

In terms of c, the speed of sound, equation (4.1) becomes

$$\frac{c_B^2}{\gamma - 1} = \frac{c_I^2}{\gamma - 1} + Pr \left(\frac{u_I^2}{2} + \frac{q_w}{\tau_w} \, u_I \right),$$ (4.2)

where we have used the equation of state for a perfect gas. Assuming that the wall is adiabatic, i.e. $q_w = 0$, (4.2) simplifies to

$$c_B^2 = c_I^2 + \tfrac{1}{2} Pr \, (\gamma - 1) \, u_I^2 \, .$$ (4.3)

The state in point B is now completely described by:

$$\begin{cases} u_B = 0 \\ v_B = 0 \\ c_B = [\, c_I^2 + \tfrac{1}{2} Pr \, (\gamma - 1) \, u_I^2 \,]^{\frac{1}{2}} \\ p_B = p_I \, . \end{cases}$$ (4.4)

In terms of $z = \ln (p \rho^{-\gamma})$, the logarithm of the entropy, the relation $p_B = p_I$ is written as :

$$z_B = z_I - 2 \, \gamma \, \ln r_c \, ,$$ (4.5)

where r_c denotes c_I / c_B. In many cases we need also the derivative of the boundary state with respect to the (given) inner state. This Jacobian reads

$$\frac{\partial \, (u_B \, , \, v_B \, , \, c_B \, , \, z_B)}{\partial \, (u_I \, , \, v_I \, , \, c_I \, , \, z_I)} = \begin{bmatrix} 0 & 0 & 0 & 0 \\ 0 & 0 & 0 & 0 \\ J_1 \, \cos \alpha & J_1 \, \sin \alpha & r_c & 0 \\ J_2 \, \cos \alpha & J_2 \, \sin \alpha & J_3 & 1 \end{bmatrix} \, ,$$ (4.6a)

with

$$\begin{cases} J_1 = \tfrac{1}{2}\,(\,\gamma - 1\,)\,Pr\,u_I\,/\,c_B \\ J_2 = 2\,\gamma\,J_1 \\ J_3 = 2\gamma\,(\,r_c^2 - 1\,)\;. \end{cases} \tag{4.6b}$$

Note that the temperature at B is always higher than the temperature at I, as one can check with (4.3). Therefore z_B is always larger than z_I.

5. THE SOLUTION METHOD

To solve the Navier-Stokes equations we solve the Euler equations with a non-zero source term as auxiliary problems. Henceforth, Ω_h will denote a grid with spacing h and $E_h^{(1)}$ the first-order discretized Euler-operator on Ω_h. The operator $N_h^{(k)}$ denotes the discretized Navier-Stokes operator, of which the Euler part is discretized to k-th order, $k=1,2$. Its viscous part is defined by the method mentioned in section 4. As it was shown there, this part is discretized with second order accuracy for vanishing grid spacings h_ξ and h_η. The discrete solution on Ω_h is given by q_h. Then, in shorthand, the discretized Navier-Stokes equations are written as

$$N_h^{(k)}(q_h) = 0\,. \tag{5.1}$$

This becomes an Euler problem when we write it as :

$$E_h^{(1)}(q_h) = E_h^{(1)}(q_h) - N_h^{(k)}(q_h)\,, \tag{5.2a}$$

which is equivalent to

$$E_h^{(1)}(q_h) = r_h^{(k)}(q_h)\,. \tag{5.2b}$$

The source term $r_h^{(k)}(q_h)$ is called the (Navier-Stokes-) defect. Note that this method of rewriting is not typical for the Navier-Stokes operator; it could have been applied to the second-order-discretized Euler operator as well; this version has been used by Hemker [8].

To define an iterative process for solving (5.2) we introduce a sequence of solutions $\{q_h^{(i)}\}_{i=0,\cdots,\infty}$, defined by

$$q_h^{(0)} := q_h^{(*)}\,, \tag{5.3a}$$

$$E_h^{(1)}(q_h^{(i+1)}) = r_h^{(k)}(q_h^{(i)}), \qquad \text{for } i=0,1,2,\cdots \tag{5.3b}$$

The iteration (5.3b) is called a Defect Correction Process (DCP). The initial solution $q_h^{(*)}$ remains to be given. Solving problems with a second order discretized Euler operator, Hemker [8] set $q_h^{(*)}$ equal to an approximation of the solution of the first-order discretized Euler equation $E_h^{(1)}(q_h)=0$. We did not use this strategy here. Instead, a new strategy was used which we shall discuss later on.

Convergence of $\{q_h^{(i)}\}_{i=0,\cdots,\infty}$ is not known a priori. However, the source term $r_h^{(i)}$ is inversely proportional with the Reynolds number. Hence, the method for solving an Euler problem with a source term is stable, convergence is guaranteed for sufficiently high Reynolds numbers.

To actually perform a DCP-cycle, we used the FAS procedure introduced by Brandt [5] for solving sets of non-linear equations within a Multi-Grid strategy. In FAS some pre- and post-relaxations are performed on each grid. Interaction between solutions on all grids is established by restrictions and prolongations. We assume the reader is familiar with FAS. We will write the FAS procedure here in an Algol-68 like form. Henceforth Ω_1 and Ω_L ($=\Omega_h$) will denote the coarsest and finest grid respectively. Furthermore, q_l denotes the solution on grid Ω_l ($l=1,...,L$).

```
procedure  FAS = ( {q_i,q_{i+1},...,q_j}, {r_i,r_{i+1},...,r_j} ) :
begin
      to pmg do relax(q_j,r_j) od ; {pre-relaxations}
      if j > i
      then
            { q_crs is a temporary solution}
            q_crs := restriction of q_j ;
            q_{j-1} := q_crs ;
            r_{j-1} := E_j^{(1)}(q_{j-1}) + restriction of (r_j - E_j^{(1)}(q_j)) ;

            to s do FAS( {q_i,q_{i+1},...,q_{j-1}}, {r_i,r_{i+1},...,r_{j-1}} ) od ;

            q_j := q_j + prolongation of ( q_{j-1} - q_crs )
      fi ;
      to qmg do relax(q_j,r_j) od {post relaxations}
end ;
```

The smoother we used was the collective symmetric Gauss-Seidel relaxation. The collective Gauss-Seidel relaxation consists of scanning the grid-cells in lexicographical ordering and solving the set of four non-linear equations for each cell, as given by (2.3). Such a set of four equations is obtained by assuming the states in the neighbouring cells to be fixed. The Gauss-Seidel relaxation is called symmetric if the grid is scanned in one direction the first time and in the reverse direction the second time. Collective symmetric Gauss-Seidel relaxation has shown good convergence in many computations.

With the help of abovementioned FAS routine, a DCP-cycle can be written as

```
procedure  DCP = ( {q_i,q_{i+1},...,q_j},{r_i,r_{i+1},...,r_j}) :
begin
      r_j := E_j^{(1)}(q_j) - N_j^{(k)}(q_j) ; {set source term to defect}
      to nfas
      do
            FAS( {q_i,q_{i+1},...,q_j},{r_i,r_{i+1},...,r_j} )
      od
end ;
```

The parameter nfas specifies how often a FAS-cycle is done in each DCP-cycle. For increasing values of nfas the solution becomes more accurate. However, it is not necessary at all to solve the Euler-problem to full precision. Because the FAS-cycle is the expensive part of the computation, this would result in a very inefficient way of finding the final solution in terms of computing time. In our experiments we observed good convergence with nfas = 1 or 2, i.e. with only one or two FAS-cycles per DCP-cycle. The results we obtained by this solution method will be discussed in the next section.

Finding the initial approximation $q_h^{(*)}$

To find $q_h^{(*)}$ we use a process which we call Viscous-Full-Multi-Grid (VFMG). This procedure starts at the coarsest grid (Ω_1) with an approximate solution. Then it performs a specified number of DCP-cycles on this grid, followed by a (second order) prolongation to the next finer grid. This process is continued until a solution on the finest grid, Ω_L, has been found. Thus we expect to have a good initial solution on Ω_L which already has some typical Navier-Stokes effects; effects which would certainly not have been obtained by setting q_L to (an approximation of) the solution of the first-order-discretized Euler equations.

The VFMG-routine is given by:

```
procedure  VFMG = ( {q_1,q_2,...,q_L},{r_1,r_2,...,r_L}) :
begin
    for j from 1 to L-1
    do
        {parameter d specifies the maximum number of grids to be used within DCP}
        integer i = maximum (1,j-d+1) ;
        to ndcp
        do
            DCP( {q_i,q_{i+1},...,q_j},{r_i,r_{i+1},...,r_j} )
        od;
        q_{j+1} := prolongation of  q_j
    od ;
    q_h^{(*)} := q_L
end ;
```

The parameter ndcp specifies the number of DCP-cycles to be performed before prolongation to a finer grid. The optimal value for this parameter is difficult to prescribe. On the one hand one is tempted to give it a large value, thus ensuring a good solution of the Navier-Stokes equations on each level. This is tempting to do since the work on a coarser grid is significantly less than on finer grids. Thus one hopes to get a good initial solution for the finer grid. On the other hand the value of the parameter ndcp can be too large since the coarser grids do not resolve high frequency phenomena that will be present in the finer grids, such as boundary layers. By this we mean that for a certain j in the VFMG procedure the norm of $N_{j+1}^{(k)}(q_{j+1})$ can be relatively large, while the norm of $N_j^{(k)}(q_j)$ (almost) vanishes. In our method we found ndcp = 1 to be satisfactory though.

There is another parameter in the VFMG-process, the parameter d. This parameter specifies the number of coarser grids that can be used in each DCP-cycle called by VFMG. In all our experiments we set d to 1, i.e. once a prolongation was made from q_j to q_{j+1}, the DCP-cycles for q_{j+1} did not use $q_1,q_2,...,q_j$. No extensive experiments were done to optimize d.

We have to stress that, however much work is done to get a good initial solution on Ω_L, the main part of all work is done by the DCP-cycles that are called after the initial solution has been found by VFMG.

A typical computation in our experiments as reported in the next section reads

```
begin {begin of run}
    ..
    ..
    q_1 := initial guess on the coarsest grid ;
    VFMG ( {q_1,q_2,...,q_L}, {r_1,r_2,...,r_L} ) ;
    to 20
    do
        DCP ( {q_1,q_2,...,q_L}, {r_1,r_2,...,r_L} )
    od ;
    ..
    ..
end {end of run}
```

6. NUMERICAL RESULTS

In the experiments reported in this section, the following choices were made:

- $k = 1$ (i.e. the first order Euler discretization was used),
- $\gamma = 1.4$,
- $Pr = 0.7$ (a typical value for air),
- the Osher scheme for the computation of the numerical Euler-flux over each volume wall.

6.1 DESCRIPTION OF THE MODELS

We performed computations on three model problems.

Model 1

Poiseuille flow between two flat parallel plates at $M=0.3$ (maximum) and Re $= 2000$. The inflow was parallel with the x-axis; the channel was 1 unit long and 1 unit high . The lower flat plate was positioned at y=0, the upper one at y=1.

The boundary conditions were : a given state at the inlet (parabolic inflow, $u(0,0)=u(0,1)=0$, $u(0,\frac{1}{2})=0.3$; $v=0$; $c=1$; $z=-\gamma\ln\gamma$) and the no-slip condition imposed at the plates as described in section 4. At the outlet the pressure was fixed at p_{out}. The pressure p_{out} was computed with a formula which had been obtained by assuming $v=0$, $u_x=0$ and u_y linear with y (parabola!). Substituting this into the incompressible Navier-Stokes equations led to the relation: $p_{out}=p_{inlet}-8\,u_{max}\,\rho_{inlet}$ / Re. The remaining state variables in a point on the outlet were computed by means of Euler-characteristics. Since for this case, subsonic outflow, three characteristics pointed outward the outlet the prescription of pressure only was enough (i.e. for the Euler equations).

Special attention was paid to the proper representation of u at the inlet. In order to achieve equal mass transport at the inflow on all grids, u was set to the mean value of a parabola over a certain interval. This parabola was $u(y)=4u_{max}y\,(1-y)$, with $u_{max}=0.3$ and the adapted u-value over the interval $[y_0-d,y_0+d]$ is given by $4u_{max}\,(y_0-y_0^2-d^2/3)$. This value is obtained by integrating $u(y)$ over the interval and dividing it by $2d$. Note that ρ is not involved in this computation since it is assumed to be constant (like in the incompressible case, which we wanted to approximate).

The initial solution was obtained by setting $q(x,y)$ equal to $q(x=0,y)$.

In the VFMG-process the parameters pmg and qmg (see description of FAS) were set to 1 and 2 respectively. The parameter nfas and ndcp were both set to 1. The coarsest grid had 4 cells in both directions, the finest 16 (see figure 7).

A total number of twenty DCP-cycles was performed after VFMG, using two FAS-cycles per DCP-cycle. Within these FAS-cycles, one pre- and two post-relaxations were used per level.

Model 2

Flow between two flat parallel plates at $M=0.85$ (maximum), and again Re $= 2000$. The inflow was parallel to the x-axis; the channel was 5 units long and 2 units high. The lower flat plate was positioned at y=0, the upper one at y=2, the inlet at x=0 and the outlet at x=5. The boundary conditions were : a given state at the inlet (u 'adapted uniform', $v=0$, $c=1$, $z=-\gamma\ln\gamma$) and the no-slip condition on the plates as described in section 4. The outlet-pressure was fixed at 0.995. As in model 1 the state in a point on the outlet was computed by means of Euler-characteristics.

By 'adapted uniform' we mean that u was specified to be 0.85 on the interval $y\in[\delta,2-\delta]$ and 0 at the no-slip walls. For $y\in[0,\delta]$ we fitted a parabola. This parabola was determined by imposing continuity for u at $y=0$ and $y=\delta$ and imposing continuity for u_y at $y=\delta$. Similarly, a parabola was fitted for the interval $y\in[2-\delta,2]$

The parameter δ is a thickness-parameter, controlling the thickness of an artificial boundary layer. It was set to 0.15. We are forced to introduce this artificial layer because solutions on several grids with

$u = 0.85$ for $y \in [0,2]$ had shown to be very different, depending on the meshsize on the finest grid. The problem lies in the points $(x,y) = (0,0)$ and $(x,y) = (0,2)$, since discontinuous boundary conditions (for u) cause a singularity at these points: the partial derivative u_y tends to infinity in their neighbourhood.

In this model the Mach number was chosen such that we expected the flow to be different from an incompressible flow (under the same circumstances).

Again, the initial solution was obtained by setting $q(x,y)$ equal to $q(x=0,y)$.

During the VFMG-process pmg and qmg (see description of FAS) were set to 1 and 2 respectively. The parameters nfas and ndcp were both set to 1. The coarsest grid had 5 cells in x-direction and 2 in y-direction. The finest grid was 40 cells long and 16 high (see figure 17). The grids were not stretched. Experiments with some stretching in the y-direction have been performed, but when the stretching became too strong, divergence of the Euler solver occurred. We were not able to explain this effect.

In total, twenty DCP-cycles were performed after the call to VFMG, using a single FAS-cycle per DCP-cycle. Within these FAS-cycles, one pre- and two post-relaxations were done.

Model 3

This is the same model as model 2, but now the lower wall between $x = 2.0$ and $x = 3.0$ is replaced by a circular bump of height 0.042 maximum (see [11] for a detailed description). This model has been considered already by many investigations for an Euler flow with full-slip boundary conditions at the upper and lower wall. The Euler simulation becomes transonic. In our Navier-Stokes simulation however we were forced to introduce an artificial boundary layer (as in model 2) which inhibited the flow to become transonic.

During the VFMG-process pmg and qmg (see description of FAS) were set to 1 and 0 respectively. The parameter nfas and ndcp were both set to 1. The coarsest and finest grid were the same as in model 2, except for the fact that a little stretching was needed to construct the bump between $x = 2$ and $x = 3$.

Again, twenty DCP-cycles were performed after the call to VFMG, using one FAS-cycle per DCP-cycle. Within these FAS-cycles, one pre- and two post-relaxations were used per level. The finest grid was 40 cells in x-direction and 16 in y-direction (see figure 27).

6.2 DISCUSSION OF THE RESULTS

Apart from a plot of the finest grid (Ω_L) and of the convergence history of the norm of the Navier-Stokes residual, the following plots were made for each model:

1. some u-profiles drawn within the channel,
2. the same u-profiles in a single plot for reasons of comparison,
3. the pressure along the lower wall and the symmetry axis of the channel,
4. the entropy, along the same two lines,
5. the Mach number along the same two lines,
6. isobars in the channel,
7. contour lines of the entropy in the channel,
8. contour lines of the Mach number in the channel and
9. streamlines in the channel.

Moreover, we plotted for model 3 the entropy distributions along the lower wall for some intermediate solutions.

Model 1

As mentioned before, this model served to check whether a flow at low Mach number (having much

resemblance with an incompressible flow) could be simulated properly.

Figure 8 shows the u-profiles within the channel. In figure 9 these profiles are superposed and from this plot it is clear that the profile that has been given as a boundary condition on the inlet, has been perfectly conserved all over the channel. This is in perfect agreement with the (incompressible) Poiseuille solution.

Figure 10 shows the distributions of the pressure along the lower wall of the channel (lower curve) and along the symmetry axis (upper curve). Both distributions appear to be perfectly linear away from the inlet. Note the scale of the pressure axis: the minimum and maximum pressure differ very little. The linearity of the pressure is in perfect agreement again with the Poiseuille flow. However, at the inlet a rather strong deviation from the Poiseuille flow has been introduced. This may be explained by a possible mismatch of the boundary conditions at the inlet and the outlet.

Figure 11 shows the entropy distribution along the lower wall. In a Poiseuille flow this distribution is linear. We suppose that the non-linearity in our results is caused by compressibility effects.

The contour plot of the entropy (fig. 14) clearly shows the generation of an entropy distribution in y-direction (the entropy was fixed at a constant value at the inlet). We deduce that for Poiseuille-like compressible flows the entropy in a flow varies in the y-direction. Note that at the outlet the entropy distribution is not yet fully developed.

The contour plot of the pressure (fig. 13) shows the structure of the steep pressure gradient near the inlet. In the middle of the channel we see that pressure mainly varies along the flow direction like in the Poiseuille flow. However, the contour lines show a slight curvature near the walls, which might be explained by a possible mismatch of the boundary condition at the inlet or outlet, or maybe even at both.

The streamlines (fig. 16), the Mach number distribution along the lower wall of the channel and along the symmetry axis of the channel (fig. 12) as well as the contour lines of the Mach number (fig. 15) show what we expect.

Figure 37 shows the convergence history. The independent variable is the number of DCP-cycles on the finest grid. Note that in each DCP-cycle 3 symmetric Gauss-Seidel relaxations were performed on each grid: one before and two after a coarse grid correction. The dependent variable is the sum of the L_1-norms of the components of the Navier-Stokes residual on the finest grid. This residual is defined as $N_h^{(1)}(q_h^{(i)})$. The mean convergence factor per DCP-cycle was 0.758.

Model 2

In fact, model 1 was a flow which was totally governed by viscous effects: the parabolic inflow type is an effect that is typically found in channel flows with friction. In model 2, we want to simulate a flow that has a large region with negligible viscous effects and two small regions with strong viscous effects, namely the two walls with the no-slip condition. As mentioned before, we first tried to simulate a flow with uniform inflow at a Mach number of 0.85, but these computations failed because these boundary conditions generate singularities in the flow at the inlet corners.

As a consequence, we were forced to make the boundary conditions continuous at the inlet and so we introduced an artificial boundary layer which could be resolved by the finest grid. Our goal with the uniformly distributed inflow was to see the birth and growth of a boundary layer. This goal could not be fully reached any more, due to our artificial boundary layer.

In figure 18 the velocity profiles at five different x-locations are shown. The profile at the inlet is continuous, as we mentioned before. Still it was not a very realistic profile since the profile had very strong variation in its derivative at the beginning of the artificial boundary. The outlet profile though, is far more physically realistic: the profile has been smoothed in y-direction. Besides this typical shear-stress effect, an influence of normal stresses (pressure) is clearly visible: the velocity variation along the channel axis. (fig 19)

The pressure distribution (fig. 20) agrees perfectly with the law of Bernoulli, which states that $p + \rho u^2 / 2$ remains constant in a one-dimensional flow. A good explanation for the steep pressure gradient near the inlet is lacking. We think that the use of a Dirichlet boundary condition for all

solution components at the inlet causes this gradient.

The entropy distribution along the lower wall (fig. 21, upper curve) shows that the entropy increase does not start with a constant gradient. This might be obtained by decreasing the Reynolds number or increasing the channel length. The distribution along the symmetry axis of the channel shows it to be constant. The increase of entropy along the lower wall is clearly visible in the contour plot of the entropy (fig. 24), which also shows the birth of an entropy distribution in y-direction, just as we saw in model 1.

Figure 23 shows the contour lines of the pressure of this model. As in model 1, it shows a steep pressure gradient near the inlet. The pressure distribution which we saw in figure 20 is visible in the isobars again. Note the strong wiggles in most contour lines. The wiggles might be explained with a possible switch from well-posed to ill-posed formulation of the boundary condition across the kinks in the velocity profile at the inlet. (These wiggles and kinks are at the same distance from the wall !)
As in model 1 the plots of the Mach number and the streamlines are what we expected (figures 22,25 and 26).

Figure 38 shows the convergence history of the Navier-Stokes residual. We see that there is faster convergence per DCP-cycle. This faster convergence is probably due to a faster convergence of the Euler solver for larger Mach numbers.

Model 3

This model, of which the Eulerian equivalent is a well-known, was used to see the influence of the bump on the flow. The Euler flow with the same inlet Mach number (0.85) is known to be transonic. For the reason mentioned before, we could not impose uniform inflow on the inlet. As a consequence, the flow remained subsonic over the whole region.

Still, the u-profile at the outlet (fig. 28) clearly shows the influence of the bump, which has thickened the boundary layer a little. In figure 29 the velocity profiles are superposed and, comparing them with model 2 we see that the difference between the maximum and minimum velocity along the symmetry-axis of the channel is larger than the corresponding difference in model 2.

The flow shows lower velocities in the lower part of the channel. This is probably due to the larger friction which the fluid experiences in this part. This is illustrated by figure 32 which shows the Mach number along a line through the centres of the lowest cells. Knowing that the speed of sound varies very little over the whole channel, the Mach number is a good indicator of the u component of the solution. (Apart from some points on the bump, the v-component is almost zero over the whole channel.)

The pressure distribution along the lower wall (fig. 30) shows a remarkably steep increase at both the leading and trailing edge of the bump. In [12] a similar effect was found with an Euler flow. There it was demonstrated that a flow over a kink may lead to zero-th order discretization errors in the Euler discretization. Here another effect is added: the error in the computation of an artificial boundary state as given by equation (3.6). Due to the erroneous pressure increases at the leading and trailing edge of the bump, the effect of the bump on the pressure distribution along the lower wall is somewhat hidden. Yet, the pressure distribution along the middle of the channel still shows some influence of the bump.

On the other hand, the Mach number distribution along the lower wall (fig. 32) clearly shows the increase and decrease of the Mach number just upstream respectively downstream $x = 2.5$, the point at which the bump has its maximum height (acceleration followed by deceleration).

Comparing the entropy distribution along the lower wall of the channel (fig. 31) with that of problem 2 (fig. 21), the extra entropy rise caused by the bump is clearly visible.

The contour plot of the pressure (fig. 33) also shows the influence of the bump. It shows a pressure distribution which is typical for subsonic flows around slender bodies. Note that there are some closed contour lines above the bump. We do not know whether these are realistic or not. Again, the kinks we mentioned in model 2 are visible in most isobars. Note that they have been smoothed away just after the bump on the lower wall. As in the models 1 and 2, this contour plot also shows steep pressure

gradients at the inlet.

The contour plot of the Mach number shows the flow to be fully subsonic. The strange contour lines in front of the bump and at the inlet could not be explained.

Comparing the contour plot of the entropy (fig. 34) with that of model 2 we see an extra entropy rise due to the bump and a thickened layer along the lower wall.

The streamlines (fig. 36) show what we expected.

The convergence history of model 3 (fig. 39) shows the fastest convergence factor per DCP-cycle.

For model 3 we made several plots of the entropy along the lower wall for some intermediate solutions that we obtained just before the 1st DCP-cycle and after the 1st, 2nd, 3rd, 5th, 10th and 20th DCP-cycle. The solution just before the first DCP-cycle is the solution we obtained with VFMG.

Figure 40 shows these plots all in one. The upper curve is the one we had after VFMG. After 1 or 2 DCP-cycles the entropy in the neighbourhood of the bump had almost totally established. The entropy towards the outlet still varied a little. The strongest variations of the entropy with respect to the number of DCP-cycles is clearly visible near the inlet. This confirmed our hypothesis that the inlet boundary condition was improperly posed; especially the assumption of constant entropy all over the inlet is doubtful.

Figures 41 through 47 show the same entropy distributions but now one curve per plot. One can easily check that no significant changes in the flow were introduced after 5 DCP-cycles. Hence we see that it is not necessary to solve the Navier-Stokes equations to full precision. In [13] Koren shows that for airfoil flows an already good solution of the second order discretized Euler equations is found after only one DCP-cycle! Of course we did not expect here such a convergence because the solution of the Navier-Stokes equations introduces essentially new effects into the solution of the Euler equations.

7. CONCLUSIONS

The overall conclusion is that it is very well possible to solve the compressible Navier-Stokes equations (at high Reynolds numbers) with a method based on defect correction. It is a method which uses the inversion of the simple discrete operator $E_h^{(1)}$ only.

If grid stretching was introduced for models 1 and 2, the convergence was bad, if present at all. The more stretching, the worse convergence was. We could not explain this.

The boundary condition for a solid wall with the no-slip condition, as derived in section 4, yields good results. We have to emphasize that a hidden assumption in the derivation of this boundary condition is that the angle between the direction of the flow near the wall and the wall itself is small, i.e. α is small. Indeed, in the models considered this was true.

The assumption that the viscous fluxes at the points on the outlet were negligible ,seems to be valid in all models: the use of Euler characteristics yields good results here.

Also at the inlet, we tried to use boundary conditions based on the Euler equations, but in these experiments the Euler solver failed to converge. Therefore we use Dirichlet conditions for all components of the solution. The consequence of this boundary condition in combination with the assumption of constant entropy along the inlet is clear: in all models a steep pressure gradient appears at the inlet.

In model 1 the parabolic inflow was perfectly conserved through the whole channel. We see that the low Mach number caused the flow to behave like an incompressible flow indeed.

From figures 41 through 47 we deduce that it is not necessary to solve the Navier-Stokes equations to full precision. After 4 or 5 DCP-cycles, no significant changes are observed any more.

8. FUTURE SUGGESTIONS

We think that the following points are possible topics for further investigations:

- In order to suppress the numerical diffusion in the Euler discretization, experiments can be refined by the use of a second order accurate Euler discretization scheme,
- a better understanding of the boundary conditions at the inlet and the outlet, which do not generate pressure shocks at the inlet,
- derivation of a boundary condition for a boundary with the no-slip condition, where the angle α (see section 4) is not small,
- optimization of the setting of the parameters in the VFMG-routine, to minimize the number of DCP-cycles that have to be performed to get a sufficiently accurate solution of the Navier-Stokes equations,
- the use of nested grids on different levels that possibly do not cover the whole region where the Navier-Stokes equations have to be solved. In [14] the use of nested grids is explained and some hyperbolic partial differential equations are solved with this technique.
- A possible next model-problem could be the flow in a channel with a bump with the no-slip condition on the bump only and full-slip at the straight walls. With such a flow one could try to simulate the flow past an airfoil.

ACKNOWLEDGEMENTS

REFERENCES

[1] SCHLICHTING, H., *"Boundary layer theory"*, Mc.Graw-Hill, 1979

[2] THOMPSON, P.A., *"Compressible fluid dynamics"*, Mc.Graw-Hill, 1972

[3] LIEPMANN & ROSHKO, *"Elements of gasdynamics"*, John Wiley & Sons, New York etc., 1957

[4] BRANDT, A., *"Multigrid solutions to steady-state compressible Navier-Stokes equations. I"*, Computing Methods in Applied Sciences and Engeneering, V , pp. 407-422, R. Glowinski, J.L. Lions (editors), North Holland Publishing Company, INRIA, 1982

[5] BRANDT, A., *"Multi level adaptive solutions to boundary volume problems"*, Math. of Comp., 31, number 138, April 1977, pp. 333-390

[6] OSHER, S., *"Upwind difference schemes for hyperbolic systems of conservation laws"*, Math. Comp. 38, pp. 339-374, 1982

[7] HEMKER, P.W., SPEKREIJSE, S.P., *"Multiple Grid and Osher's scheme for the efficient solution of the steady Euler equations"*, Report NM-R8507, CWI, Amsterdam, 1985

[8] HEMKER, P.W., *"Defect correction for higher order schemes for the multigrid solution of the steady Euler equations"*, Report NM-R8523, CWI, Amsterdam, 1985

[9] HEMKER, P.W., SPEKREIJSE, S.P. *"Multiple grid and Osher's scheme for the efficient solution of the steady Euler equations"*, Appl. Num. Math., to appear

[10] PEYRET, R., TAYLOR, T.D., *"Computational methods for fluid flow"*, Springer-Verlag, New York, Heidelberg, Berlin, 1983

[11] RIZZI, A., VIVIAND, H., eds., *"Numerical methods for the computation of inviscid transonic flows with shock waves"*, Proceedings GAMM Workshop, Stockholm, 1979, Vieweg Verlag, 1981

[12] KOREN, B., *"Euler flow solutions for a transonic wind-tunnel section"*, Report NM-R8601, CWI, Amsterdam, 1986

[13] KOREN, B., *"Evaluation of second order schemes and defect correction for the multigrid computation of airfoil flows with the steady Euler equations"*, Report NM-R8616, CWI, Amsterdam, 1986

[14] BERGER, M.J., OLIGER, J., *"Adaptive mesh refinement for hyperbolic partial differential equations"*, J. of Comp. Physics 53, pp. 484-512, 1984

the regular grid   the irregular grid
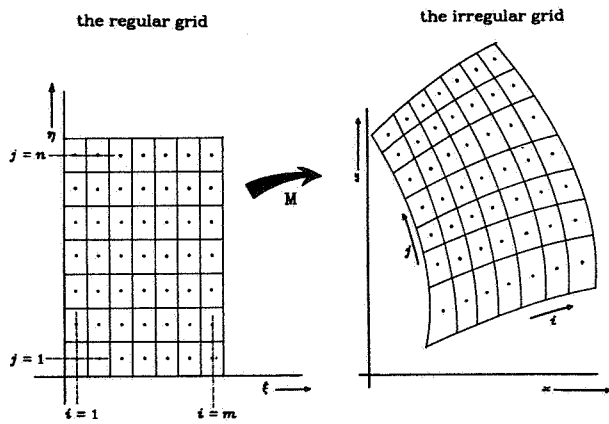
Figure 1   Example of a mapping.

----- : mapping of the regular grid
——— : discretized grid
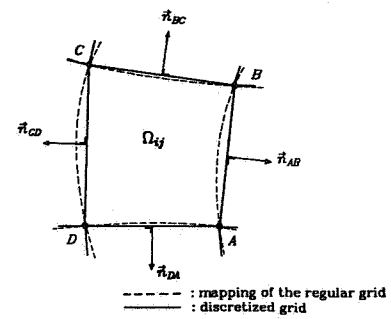
Figure 2   A finite volume
in the irregular grid.
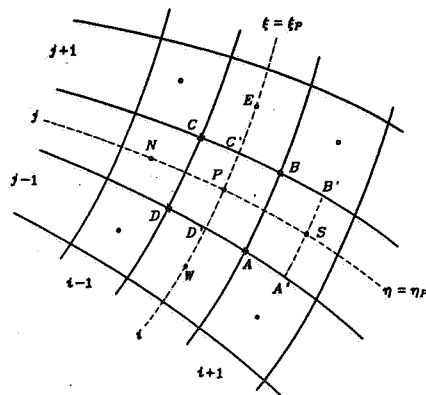
Part of the irregular grid.

Figure 3

(BC : apply boundary condition)
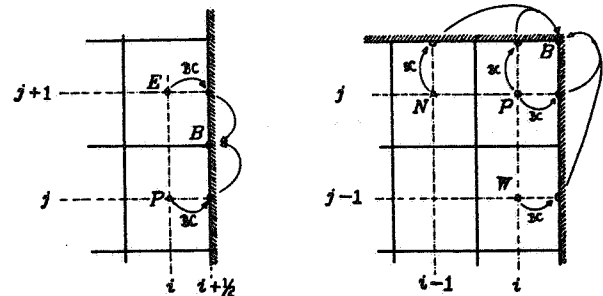
Figure 4   Treatment of the boundaries.
Figure 5   Treatment of a corner.
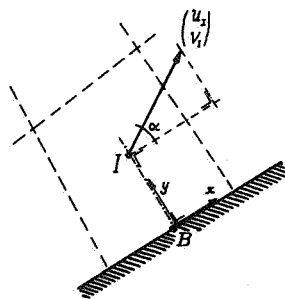
Figure 6   A state near
a boundary.
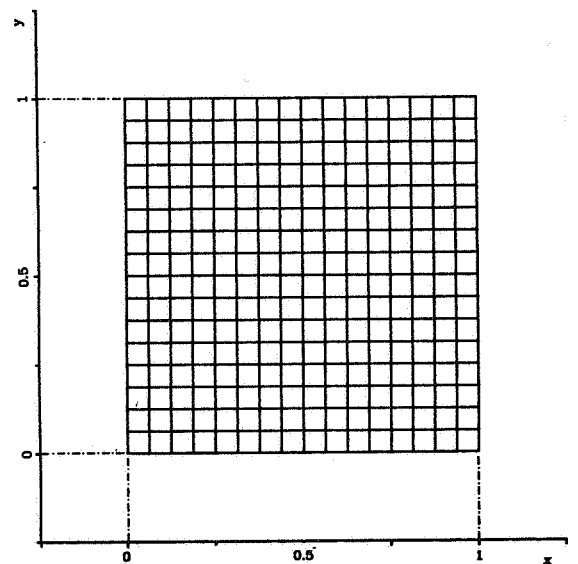
Model 1, finest grid; 16 x 16 cells

Figure 7
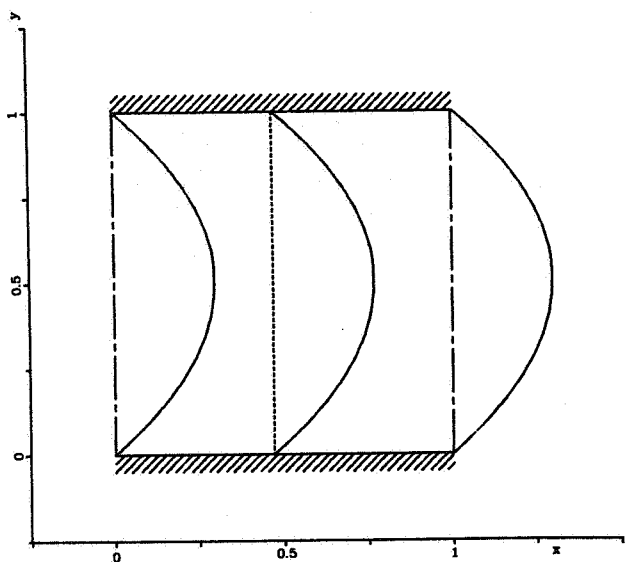
Model 1, u–profile at three locations.

Figure 8
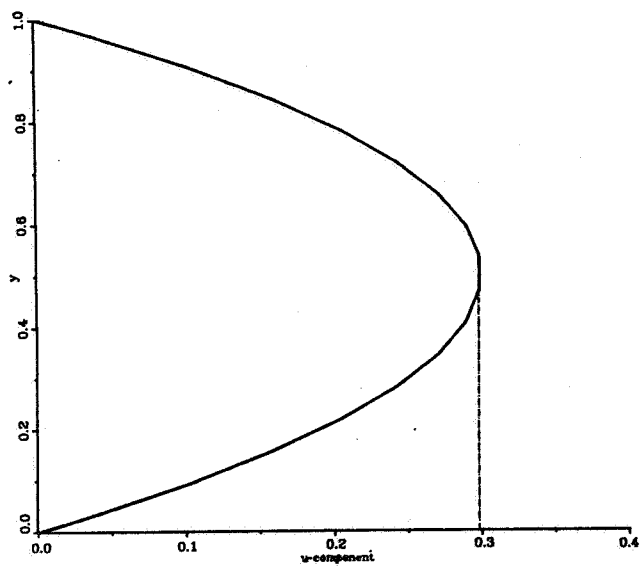
Model 1, superposed u–profiles of fig. 8

Figure 9
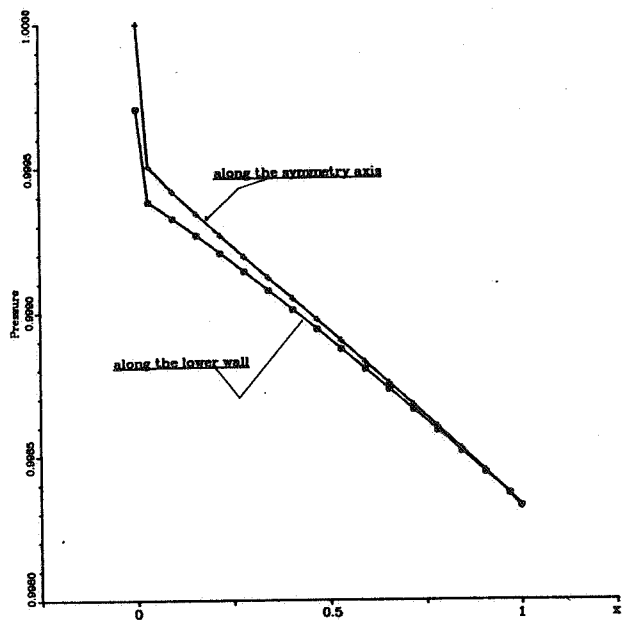
Figure 10   Model 1, the pressure
along two lines.
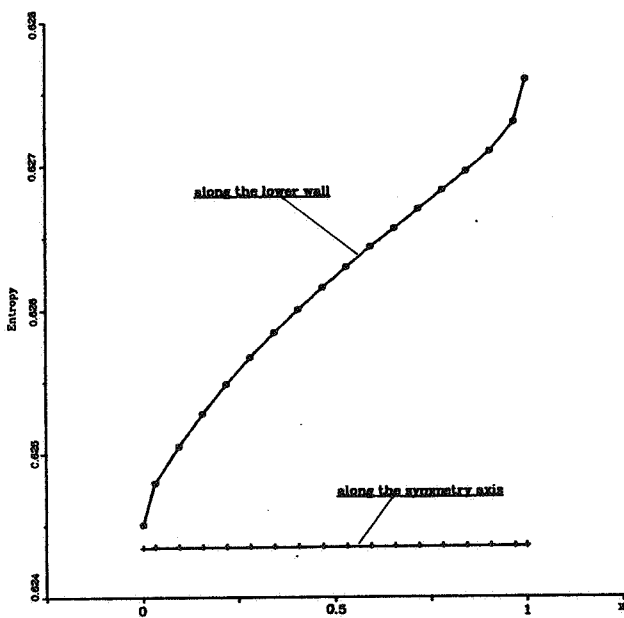
Figure 11   Model 1, the entropy
along two lines.
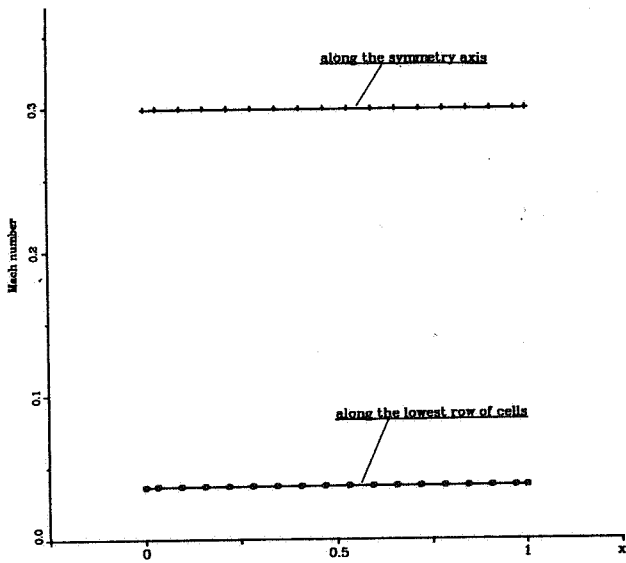
Figure 12   Model 1, the Mach number along two lines.
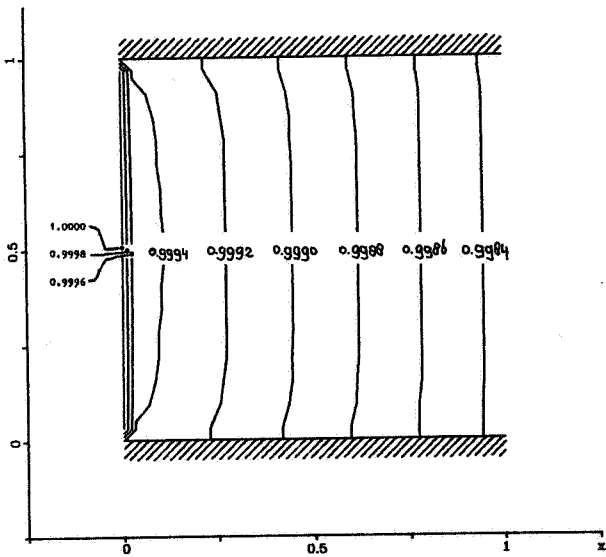
Figure 13   The isobars of model 1.

Figure 14   Some lines of equal entropy in model 1.

Figure 15   Lines of equal Mach number in model 1.
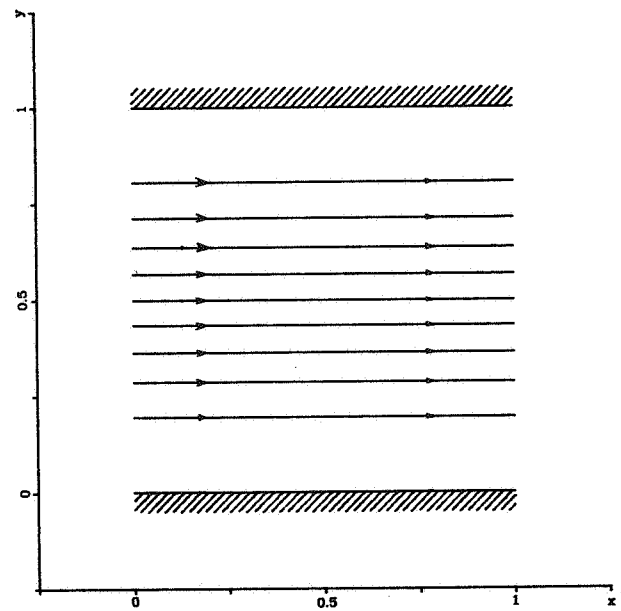
Figure 16   The streamlines of the flow in model 1.
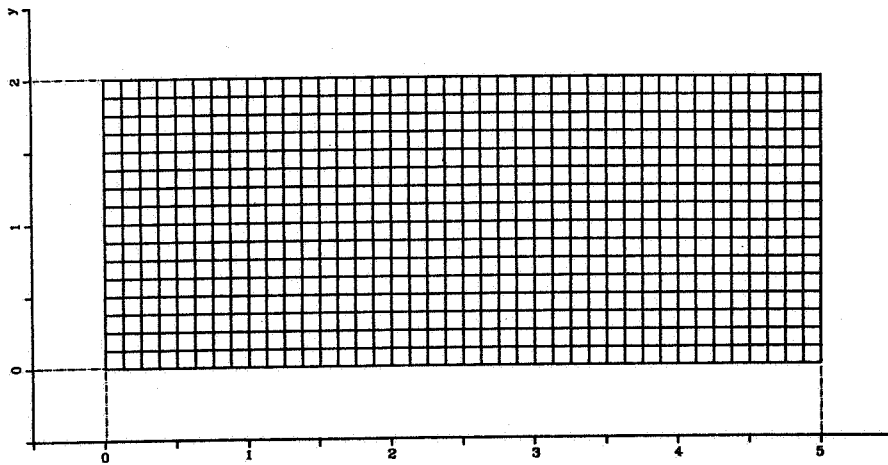
Figure 17   Model 2, finest grid; 40 x 16 cells.
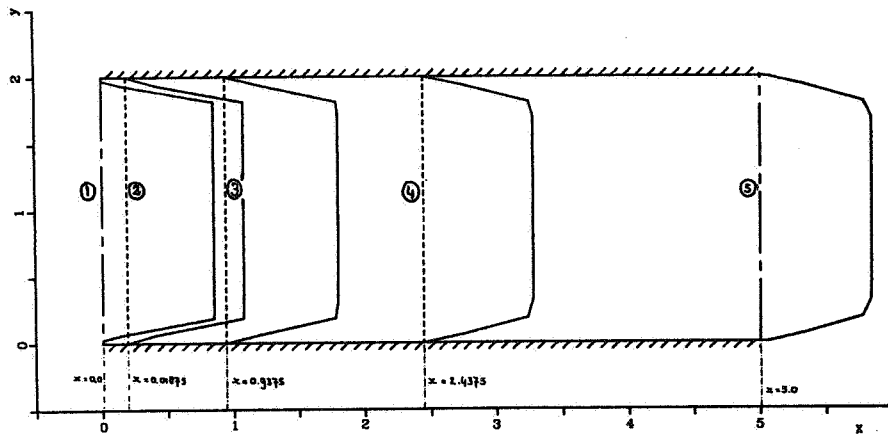
Figure 18   Model 2, u-profile at five locations.
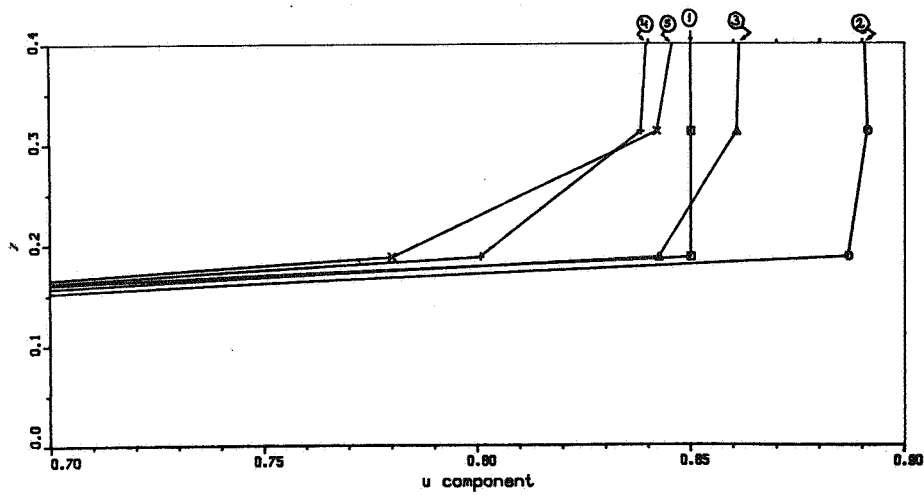
Figure 19   Model 2, superposed u-profiles of fig. 18.
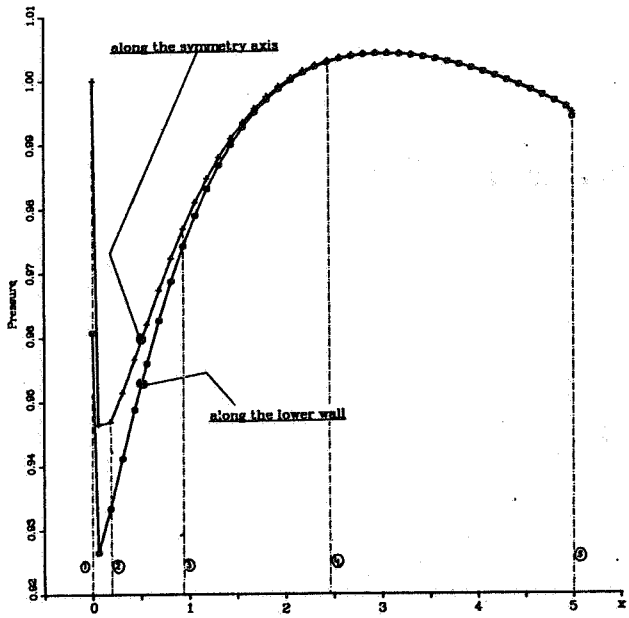
Figure 20   Model 2, the pressure along two lines.
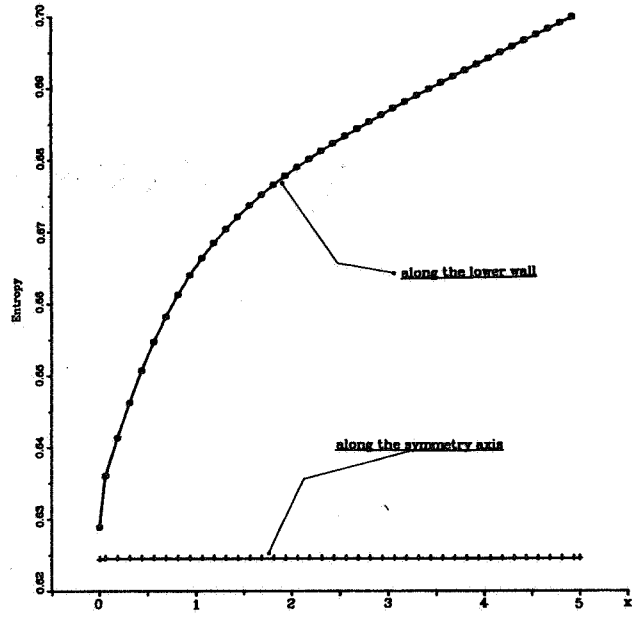
Figure 21   Model 2, the entropy along two lines.
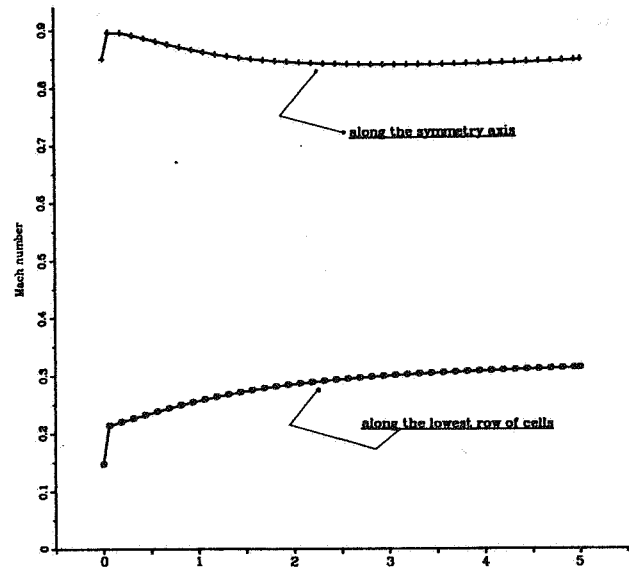
Figure 22   Model 2, the Mach number along two lines.
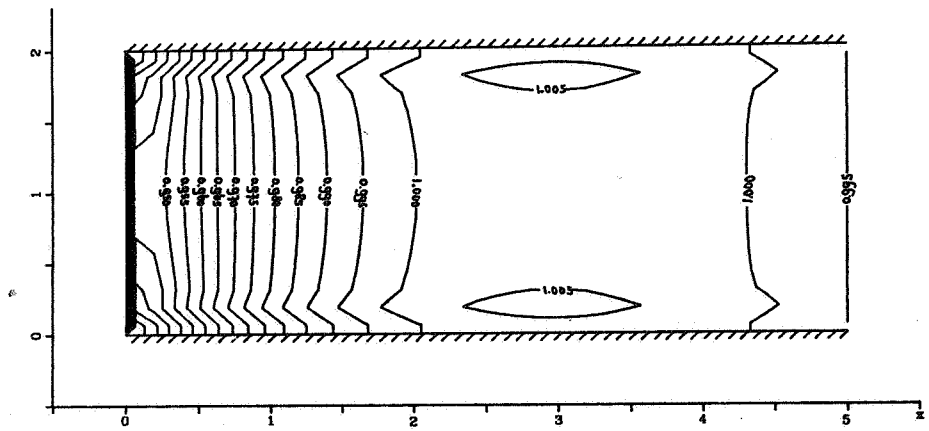
Figure 23   The isobars of model 2.
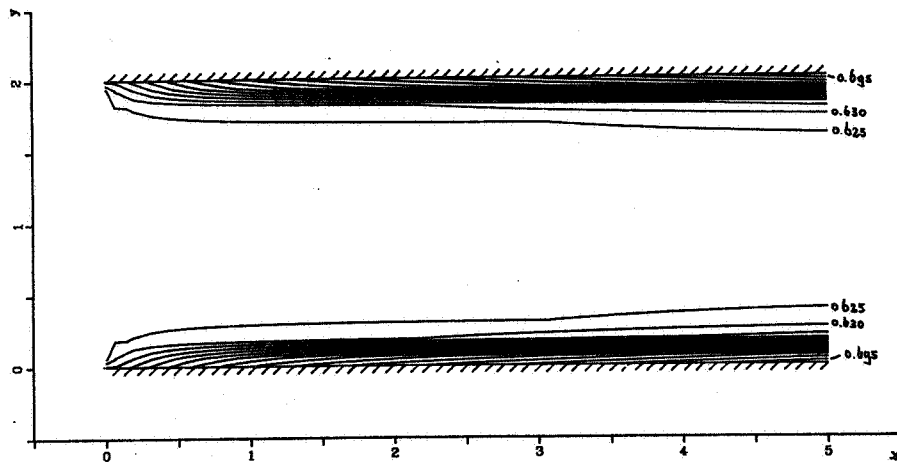
Figure 24   Some lines of equal entropy in model 2.
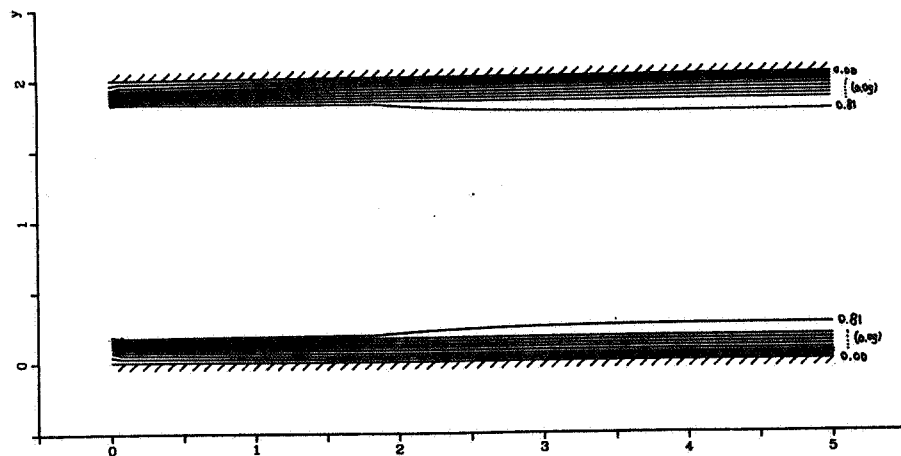
Figure 25   Lines of equal Mach number in model 2.
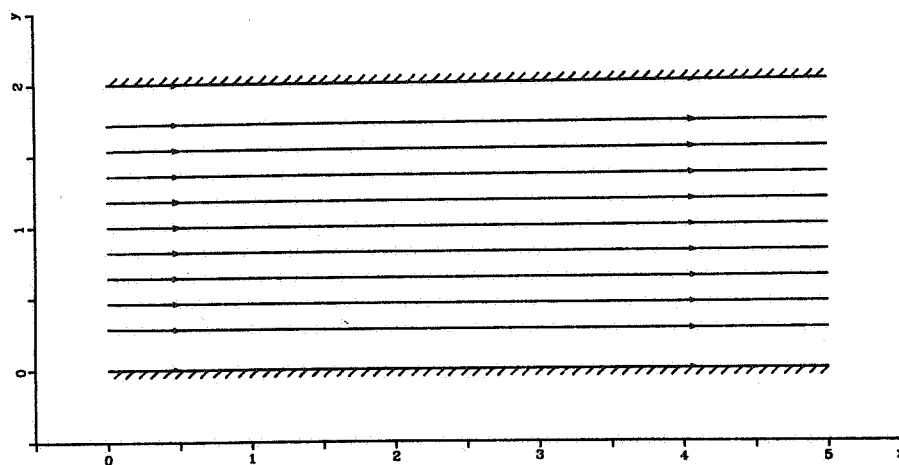
Figure 26   The streamlines of the flow in model 2.
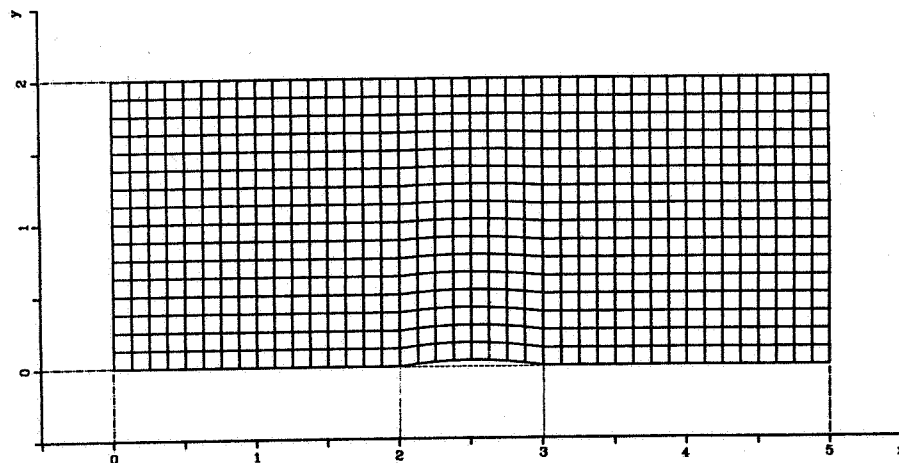
Figure 27   Model 3, finest grid; 40 x 16 cells.
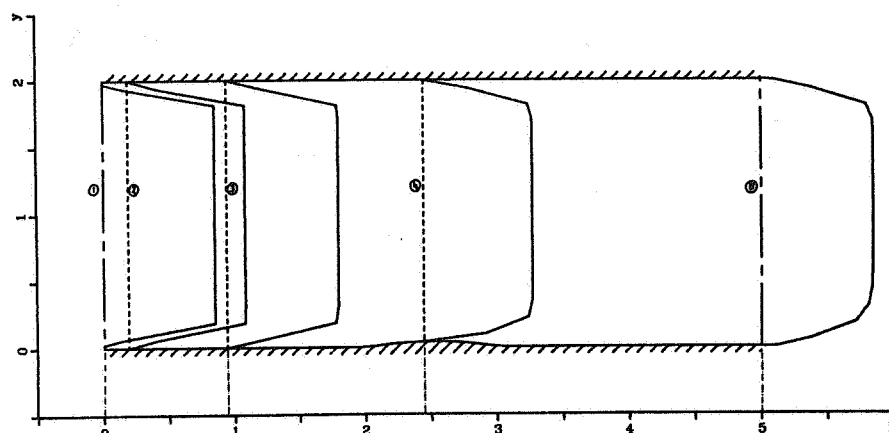
Figure 28   Model 3, u-profile at five locations.
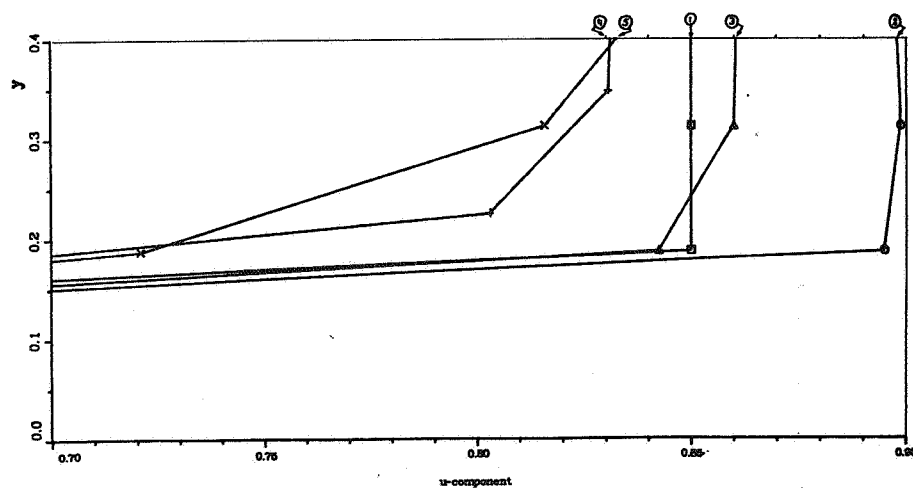
Figure 29   Model 3, superposed u-profiles of fig. 28.
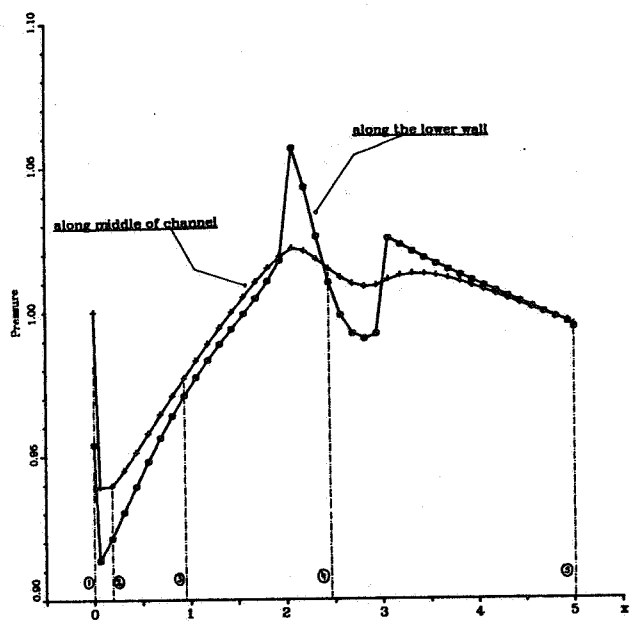
Figure 30   Model 3, the pressure along two lines.
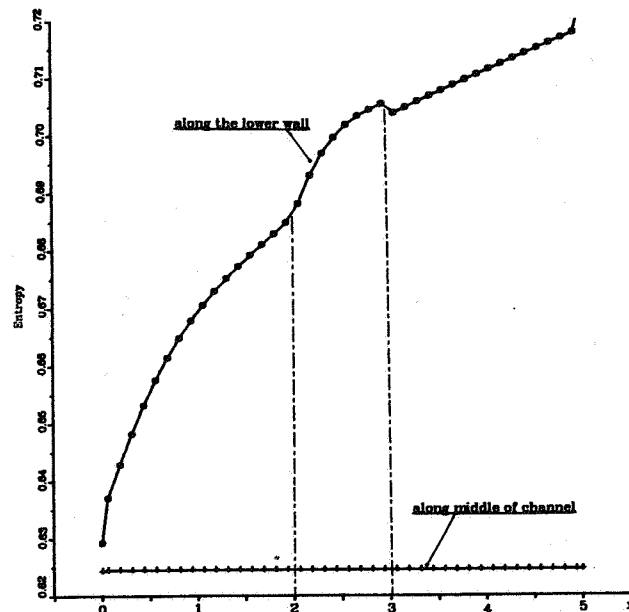
Figure 31   Model 3, the entropy along two lines.
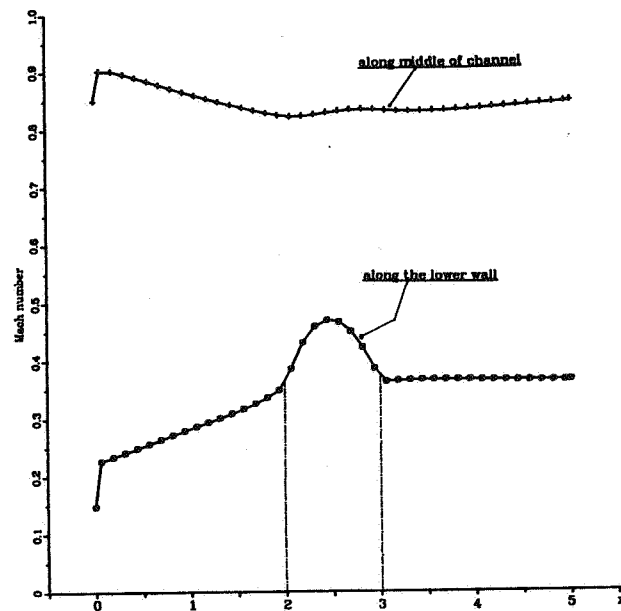
Figure 32   Model 3, the Mach number along two lines.
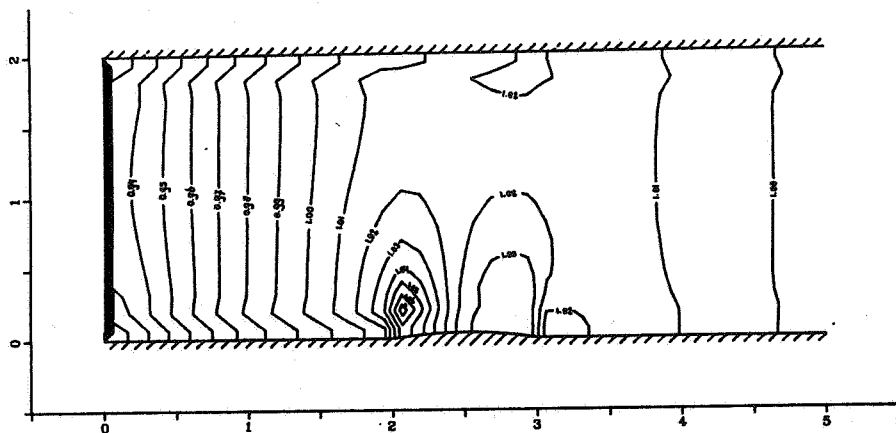
Figure 33   The isobars of model 3.
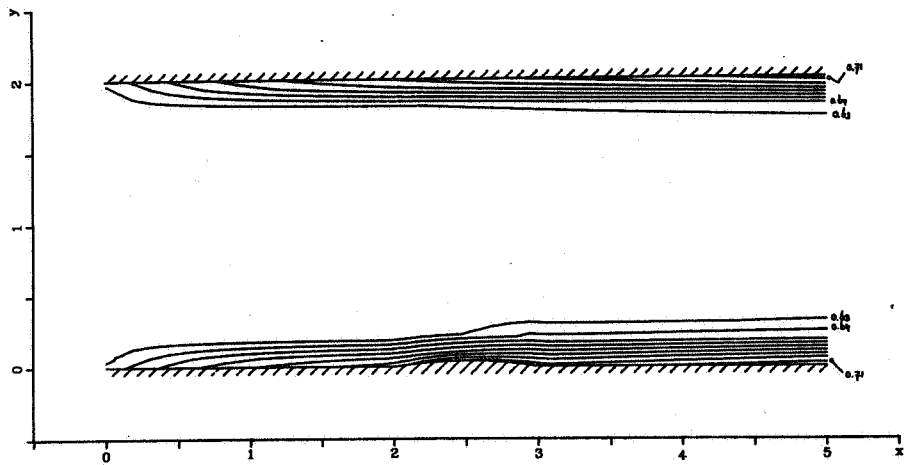
Figure 34   Some lines of equal entropy in model 3.
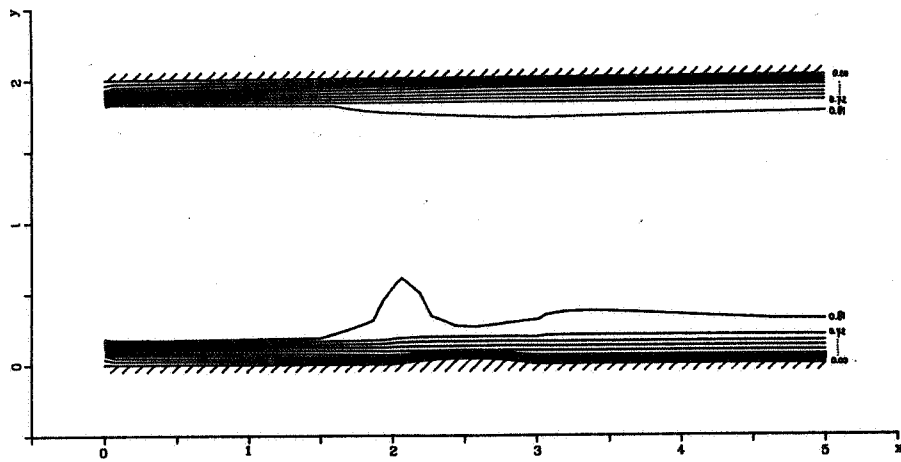
Figure 35   Lines of equal Mach number in model 3.
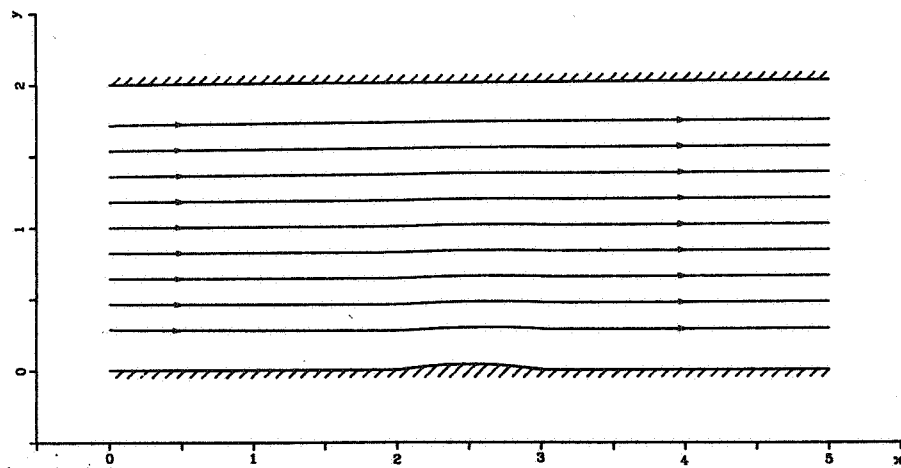
Figure 36   The streamlines of the flow in model 3.
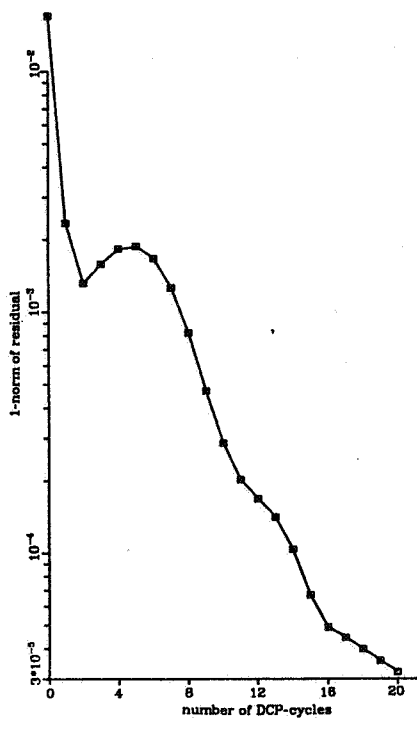
Mean reduction factor per DCP-cycle : 0.758
and mean factor per Seidel sweep : 0.955

Convergence history for model 1.

Figure 37
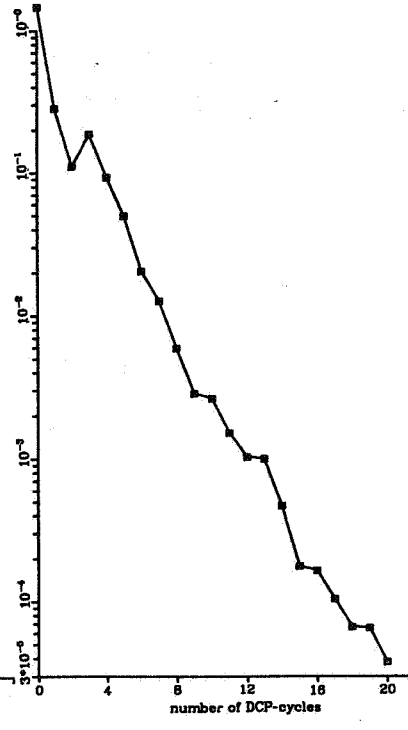
Mean reduction factor per DCP-cycle : 0.606
and mean factor per Seidel sweep : 0.920

Convergence history for model 2.

Figure 38
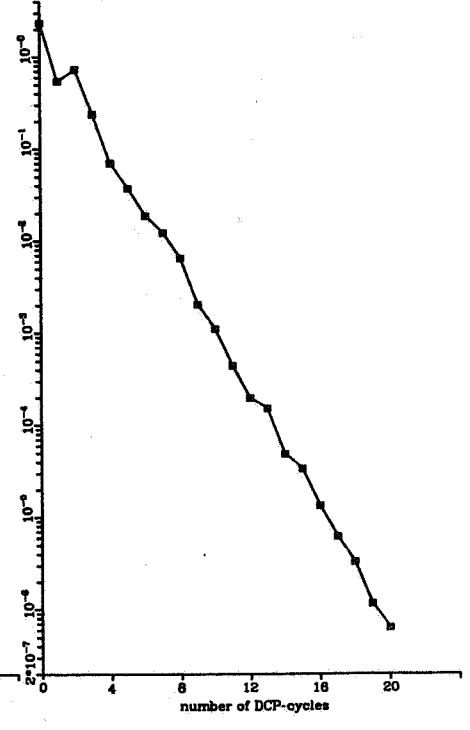
Mean reduction factor per DCP-cycle : 0.475
and mean factor per Seidel sweep : 0.883

Convergence history for model 3.

Figure 39
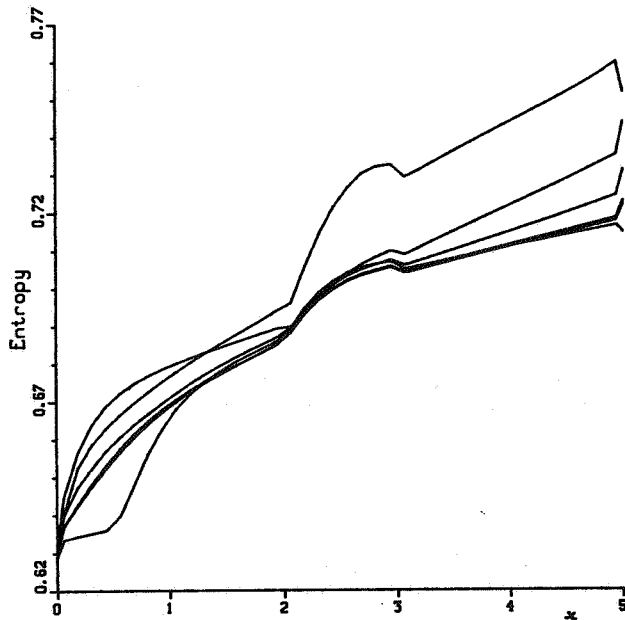
Entropy distribution for model 3. Frames 0
through 6 are superposed in this figure.

Figure 40
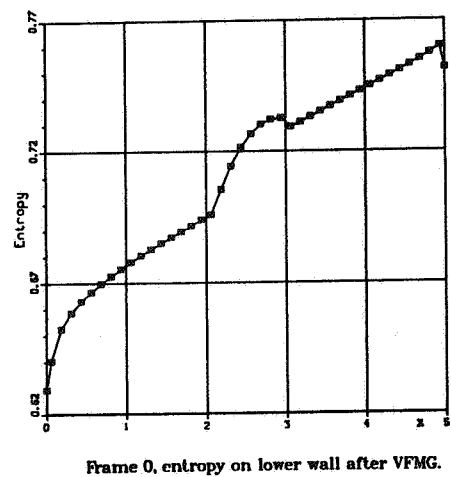
Frame 0, entropy on lower wall after VFMG.

Figure 41
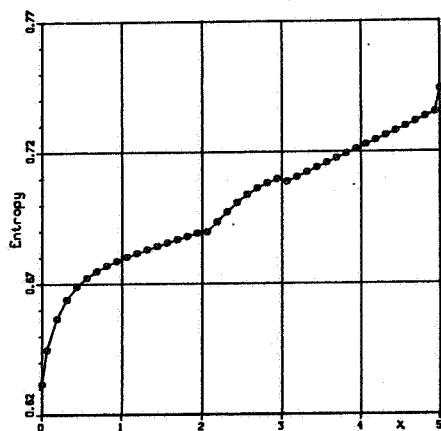
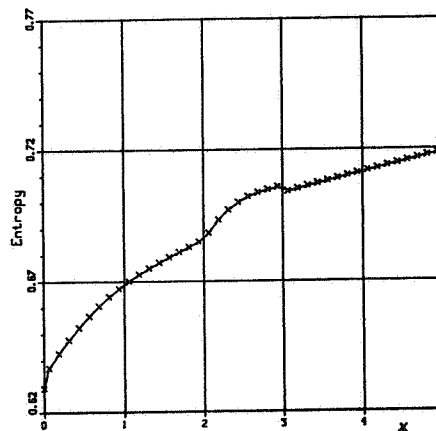Frame 1, entropy on lower wall after 1 DCP.

Figure 42
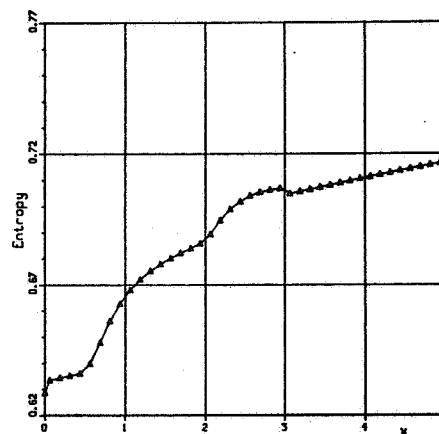
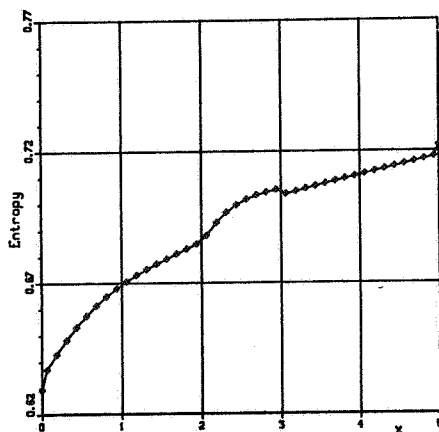Frame 2, entropy on lower wall after 2 DCPs.

Figure 43
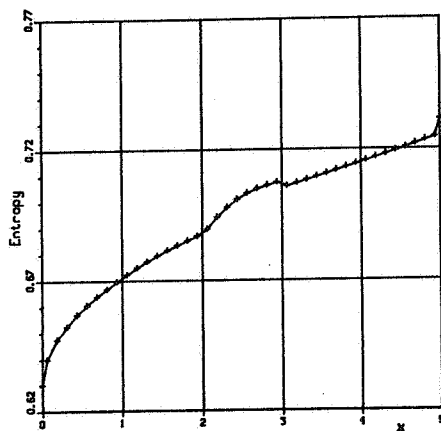
Frame 3, entropy on lower wall after 3 DCPs.
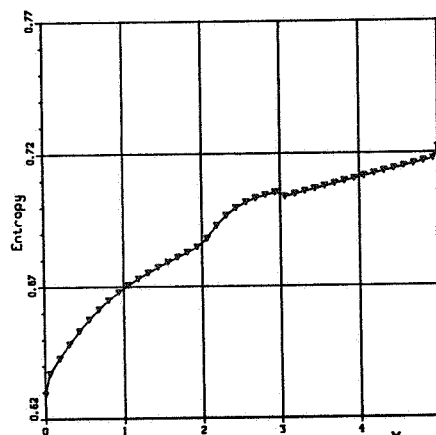
Figure 44

Frame 4, entropy on lower wall after 5 DCPs.

Figure 45

Frame 5, entropy on lower wall after 10 DCPs.

Figure 46

Frame 6, entropy on lower wall after 20 DCPs.

Figure 47